Automotive Science and Engineering, Vol. 16, No. 2, (2026), 5024-5041

Iran University of Science and Technology

Automotive Science and Engineering

Journal Homepage: ase.iust.ac.ir

ISSN: 2008-9899

Integrated Optimization of Ride Comfort and Battery Degradation in Pure Electric Vehicles with Active Suspension

Mohammad Ali Rahbari[1], Mohammad Salehpour[2*], Moharam Bahramkhoo[3], Sina Gohari Rad[4], Ali Alijani[5]

[1,2,3,5] Department of Mechanical Engineering, BaA.C., Islamic Azad University, Bandar Anzali, Iran

[4] Department of Mechanical Engineering, Ra.C., Islamic Azad University, Rasht, Iran

ARTICLE INFO

Article history:

Received : 27 Dec 2025

Accepted: 25 Apr 2026

Published: 3 May 2026

Keywords:

Pure electic vehicle

Aging

Active suspension

Optimization

Comfort ride

A B S T R A C T

This study proposes an integrated optimization framework for a pure electric vehicle equipped with an active suspension system, in which a genetic algorithm (GA) is used to optimize the membership functions of a fuzzy suspension controller by simultaneously considering ride comfort, suspension travel, battery state of charge, and battery degradation. The electric powertrain, battery aging model, and full-car active suspension model are integrated within a unified simulation environment and evaluated under NEDC, UDDS, and WLTP Class 3 driving cycles. The optimized controller improves ride comfort by up to 15.32% and reduces battery degradation by up to 5.17% compared with the non-optimized controller. The results also show reduced suspension travel while maintaining acceptable battery energy behavior. These findings indicate that incorporating battery degradation into active-suspension optimization can improve vehicle dynamic performance without imposing an excessive penalty on battery health.

1. Introduction

Electrified vehicles, including battery electric vehicles (BEVs), hybrid electric vehicles, and fuel cell electric vehicles (FCEVs), are promising solutions for reducing the environmental impact of road transportation [1]. These vehicles use batteries, fuel cells, or hybrid energy sources to supply electric propulsion and support regenerative braking [2]. Their performance depends strongly on energy management, battery usage, driving conditions, and vehicle dynamics [3]. Therefore, advanced control and optimization methods are needed to improve energy efficiency, preserve energy-storage system health, and maintain vehicle performance and passenger comfort [4].

Active and semi-active suspension systems are widely used to improve ride comfort, handling stability, and driving safety under varying road and operating conditions. Recent studies have explored several advanced control approaches. PPO-based reinforcement learning has been applied to semi-active suspension control using body acceleration, suspension deflection, and dynamic tire load as state variables [5]. MPC with road preview and an LPV half-car model has also demonstrated improved performance over passive suspension systems [6]. In addition, aperiodic

*Corresponding Author
Email Address: Mohammad.Salehpour@iau.ac.ir
https://doi.org/10.22068/ase.2026.750

[DOI: 10.22068/ase.2026.750]

sampled-data H_∞ control has been used to improve vibration suppression under model uncertainty [7], while skyhook–ADRC control has enhanced MR-damper suspension performance under different road profiles [8]. Event-triggered fault-tolerant control has also been proposed to maintain vibration suppression in the presence of actuator faults [9]. Recent research has also addressed robustness against system uncertainties in suspension control. A robust fuzzy sliding-mode controller was developed for a nonlinear full-vehicle semi-active suspension system, demonstrating the capability of the control strategy to maintain ride and handling performance in the presence of vehicle-parameter uncertainties [10]. In addition, fuzzy and genetic-algorithm-based controller optimization has been investigated for active suspension applications, showing that optimization of controller parameters can effectively improve frequency-dependent ride-comfort performance under different road excitation conditions [11]. Several studies have investigated multi-objective optimization and intelligent control methods for improving vehicle dynamic performance. A Pareto-based differential evolution approach with adaptive mutation was proposed for vehicle vibration optimization under random road excitation [12]. Subsequently, a fuzzy inference-based adaptive mutation strategy (MODE-FM) was developed to enhance the optimization of nonlinear vehicle models [13]. In addition, an optimized sliding mode controller based on the skyhook model was presented for vibration reduction in nonlinear vehicle systems [14].

Battery aging is one of the major challenges in hybrid and pure electric vehicles, as it directly affects driving range, power availability, charging capability, operating cost, and long-term reliability. Since the battery pack is among the most expensive components of an electrified powertrain, degradation caused by repeated charge/discharge cycles, high C-rate operation, deep cycling, and elevated temperature can significantly reduce both technical performance and economic viability. Recent studies have therefore emphasized the need for battery-health-aware modeling and control. One study employed a DNN-based aging predictor combined with NSGA-II optimization to balance V2G revenue and battery degradation, showing that charging rate, charging time, V2G operation, and ambient temperature strongly influence battery health [15]. Another investigation evaluated EV battery aging over a 10-year period under real driving and environmental conditions, including temperature, humidity, and solar irradiation, reporting approximately 7% total capacity loss [16]. In addition, a real-driving lithium-ion battery aging dataset based on UDDS profiles was developed using 23 months of cell testing under different charging rates and periodic capacity, HPPC, and EIS diagnostics, supporting aging model development and battery management strategies [17]. Furthermore, an enhanced TCN–SVN quantile regression model was proposed for EV lithium-battery life prediction, improving battery health estimation, remaining useful life prediction, and temperature forecasting for battery management applications [18].

Several studies have examined the integration of active or regenerative suspension systems with hybrid and electric vehicle platforms, mainly from the perspectives of ride comfort, fuel economy, handling performance, and energy recovery. A combined hybrid electric vehicle and active suspension simulation framework was developed in [19], showing that regenerative suspension energy and hybrid energy storage can reduce battery load fluctuations. In [20], a power-split hybrid electric vehicle equipped with suspension energy regeneration was investigated, demonstrating improvements in both fuel economy and ride comfort. An integrated

[DOI: 10.22068/ase.2026.750]

battery electric vehicle model with an energy-harvesting active suspension system was presented in [21] to analyze the interaction between suspension energy recovery and EV power flow. Similarly, a regenerative active suspension system for an in-wheel-motor electric vehicle was studied in [22], with emphasis on residual suspension energy recovery. Moreover, active suspension performance in an electric vehicle conversion platform was evaluated in [23], highlighting its role in improving ride and handling after changes in vehicle mass distribution. Although these studies addressed energy recovery, ride comfort, and handling performance, battery aging was not directly considered as an optimization objective. Therefore, the present study addresses this gap by jointly optimizing ride comfort and battery degradation in a pure EV active suspension framework.

Based on the identified research gap, the present study proposes an integrated optimization framework for a pure electric vehicle equipped with an active suspension system. Unlike previous studies that mainly considered ride comfort, handling, energy recovery, or battery aging separately, this work simultaneously optimizes passenger ride comfort and battery degradation within a unified simulation environment. The active suspension controller is tuned to reduce body vibration and suspension travel while limiting its negative impact on battery health. To evaluate the robustness of the proposed approach under different driving patterns, three standard drive cycles are considered: UDDS, WLTP Class 3, and NEDC.

The remainder of this paper is organized as follows. Section 2 presents the main electric vehicle models, including the battery, electric motor, and driving-cycle definitions. Section 3 describes the active suspension system and control structure. Section 4 introduces the proposed GA-based fuzzy optimization framework and objective function. Section 5 presents and discusses the simulation results under different driving cycles. Finally, Section 6 summarizes the main conclusions and future research directions.

2. Vehicle Description

Figure 1 illustrates the main architecture and energy-flow mechanism of a pure battery electric vehicle (BEV). In this configuration, the battery pack acts as the only onboard energy source and supplies high-voltage DC power to the inverter/power electronics unit. The inverter converts the DC power into controlled AC power for the electric traction motor, which then produces the required driving torque. This torque is transmitted to the driven wheels through a single-speed reduction gearbox and differential. During charging, electrical energy enters the vehicle through the charging port and is managed by the onboard charger before being stored in the battery pack. The DC-DC converter steps down the high-voltage battery output to supply the 12 V auxiliary battery and low-voltage electrical loads. In addition, the thermal management system regulates the temperature of the battery, motor, and power electronics to maintain safe and efficient operation. The longitudinal motion of the vehicle is determined by the balance between the traction force and the main resistive forces, including aerodynamic drag, rolling resistance, road-grade resistance, and inertial force. Therefore, the required wheel traction force can be expressed as:

$$P_m\eta_T\eta_{md} = (\underbrace{M\delta a_{req}}_{F_i} + \underbrace{Mgsin\alpha}_{F_{St}} + \underbrace{Mfgcos\alpha}_{F_{Ro}} + \underbrace{\frac{1}{2}\rho u^2 C_D A}_{F_L}) \tag{1}$$

In the vehicle model, (M) is defined as the equivalent vehicle mass and includes the contribution of all onboard subsystems, such as the fuel cell system, battery pack, electric motor, drivetrain elements, and auxiliary equipment. The variable (P_m) indicates the electrical power delivered to the DC/AC inverter, which is then converted into the

[DOI: 10.22068/ase.2026.750]

required form to operate the traction motor. The efficiencies associated with power transmission and motor-drive conversion are represented by (η_T) and (η_md), respectively. The remaining parameters describe the vehicle operating condition and resistive characteristics: (u) denotes the longitudinal vehicle speed, (ρ) is the ambient air density, (δ) accounts for the influence of rotating components on the equivalent mass, (A) represents the frontal area, (C_D) is the aerodynamic drag coefficient, (f) is the rolling resistance coefficient, and (g) is the gravitational acceleration. The numerical values and technical specifications adopted for these parameters are summarized in Table 1.

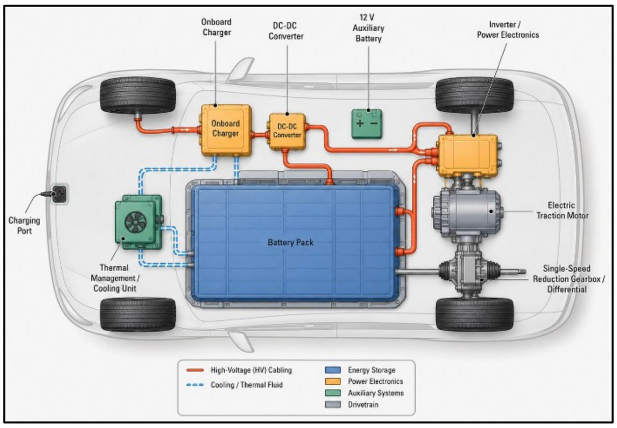

Figure 1. Structure of a FCHEV

Table 1: The specification of studied electric vehicle

	Parameters	Value	Unite
Vehicle Specifications	Drag coefficient (C_D)	0.335	-
	Coefficient of Rolling Friction (f)	0.009	-
	Front view area (A)	2.0	m^2
	vehicle Weight (M)	1144	Kg
	Effect coefficient of rotating objects (δ)	1.08	-
Battery	Nominal capacity	50	Ah
	Voltage	413	V
	Nominal energy	20.65	kWh
Motor	Maximum power	75	KW
	Maximum torque	280	Nm
	Maximum speed	10000	rpm

2.1. Battery Modeling

In this study, the battery behavior is represented using the internal-resistance-based model implemented in ADVISOR [24]. The corresponding equivalent electrical circuit, illustrated in Figure 2, describes the battery as an ideal open-circuit voltage source connected in series with an internal resistance. This formulation enables the terminal voltage and power response of the battery to be estimated under different operating conditions. Both the open-circuit voltage and the resistance are treated as variable parameters rather than fixed constants, since their values depend on the battery state of charge, operating temperature, and current direction. Therefore, separate characteristics are considered for charge and discharge modes to reflect the asymmetric behavior of the battery during energy storage and energy delivery.

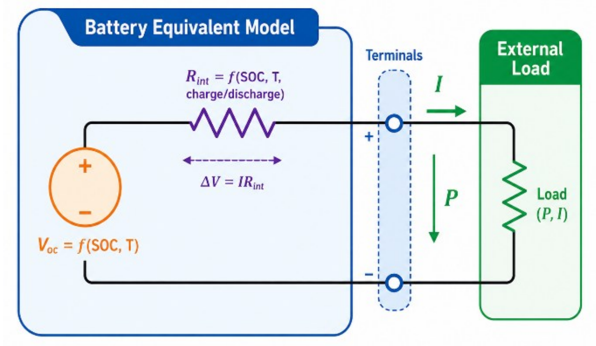

Figure 2. Internal resistance model schematic

In addition to instantaneous electrical behavior, the battery pack is affected by long-term aging as a result of repeated charge and discharge operation. This aging process gradually reduces the available capacity of the battery [25]. In this study, the battery capacity degradation is represented by the capacity fade ratio, (L_B), which compares the remaining usable capacity with the initial rated capacity [26]:

$$L_B(\%) = 100 \cdot \frac{Q_0 - Q_{rem}}{Q_0} \quad (2)$$

where (Q_0) is the nominal capacity of the fresh battery, and (Q_{rem}) represents the remaining capacity after the battery has experienced cycling over time. The accumulated electrical usage of the battery is described by the total ampere-hour throughput, (AH_{tot}). This quantity measures the total absolute charge

[DOI: 10.22068/ase.2026.750]

that has passed through the battery during both charging and discharging processes and is calculated as [27]:

$$AH_{tot} = \int_0^t |I_{bat}(t)| d\tau \qquad (3)$$

where (I_{bat}) is the battery current at time (τ). The absolute value is used because both charging and discharging contribute to battery cycling and aging.

To obtain a more realistic estimation of battery degradation, the capacity loss model is extended by including the effects of state of charge variation and operating temperature. The degradation model is expressed as [28]:

$$L_B = \Upsilon_c(SOC_{min}, r_{SOC}) \times \exp\left(\frac{-E_a}{R_g T}\right) \times (AH_{tot})^{\xi} \qquad (4)$$

In this formulation, (SOC_{min}, r_{SOC}) is a stress severity function that depends on the minimum state of charge, (SOC_{min}), and the SOC swing ratio, (r_{SOC}). The exponential term accounts for the temperature-dependent nature of the degradation mechanism, where (E_a) is the activation energy, (R_g) is the universal gas constant, and (T) is the battery operating temperature. The exponent (ξ) is an empirical parameter that adjusts the nonlinear relationship between capacity loss and accumulated ampere-hour throughput. Therefore, the model relates battery aging not only to the amount of processed charge, but also to the operating SOC window and thermal condition of the cell.

2.2 Electric Motor Modeling

The traction motor is characterized by three main operating quantities: shaft speed, generated torque, and energy conversion efficiency. In the present model, the motor is not represented by a fixed efficiency value; instead, its performance is obtained from a speed–torque efficiency map, as shown in Figure 3. This map provides the efficiency of the motor over a wide range of operating points and separates the machine behavior into motoring and generating regions. Positive torque operation, located in quadrant I, corresponds to vehicle propulsion, where electrical energy is converted into mechanical power at the wheels. In contrast, negative torque operation in quadrant IV represents regenerative braking, during which the motor works as a generator and converts part of the vehicle kinetic energy back into electrical energy. The figure also defines the allowable operating envelope of the motor by showing the maximum torque limits at different rotational speeds.

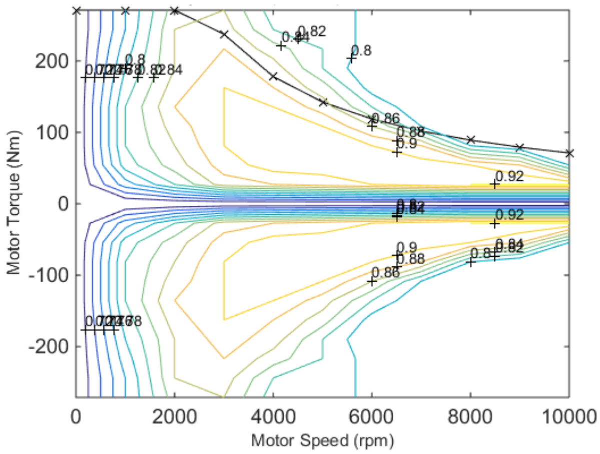

Figure 3. Efficiency map and torque-speed profile

2.3 Driving Cycle Selection and Road Input Modeling

Three standard driving cycles, namely UDDS, WLTP, and NEDC, are used in this study to evaluate the electric vehicle under different operating conditions. Fig. 4 shows the driving cycles and the corresponding road disturbance inputs used for the EV–active suspension simulations. The upper row presents the vehicle speed profiles for UDDS, WLTP Class 3, and NEDC. These cycles were selected to represent different driving conditions: UDDS mainly represents urban stop-and-go driving with frequent acceleration and braking, WLTP Class 3 includes wider speed variations and higher-speed operation, and NEDC combines

[DOI: 10.22068/ase.2026.750]

repeated low-speed urban sections with a smoother extra-urban part. Therefore, the three cycles provide different traction power demands and different excitation patterns for evaluating both battery aging and ride comfort.

The lower row of Figure 4 shows the generated road displacement inputs for the front and rear wheels under each drive cycle. The road disturbance was obtained by combining the speed profile of each drive cycle with a measured or predefined road profile. First, the drive-cycle speed was converted from mph to m/s and resampled with a fixed time step of 0.02 s. Then, the travelled distance of the front wheel was calculated by integrating the instantaneous vehicle speed over time. This distance was used to select the corresponding road elevation from the road profile. Since the road profile has a finite length, a wrapping method was applied so that the same road profile could be repeated over the complete driving cycle. The rear-wheel road input was generated from the same road profile, but with a spatial delay equal to the wheelbase, (L = 2.63) m. As a result, the rear wheel experiences the same road disturbance after the vehicle travels one wheelbase distance. When the vehicle speed becomes almost zero, both front and rear road inputs are set to zero, representing the absence of road excitation during stopping periods (for more information please refer to Table 2).

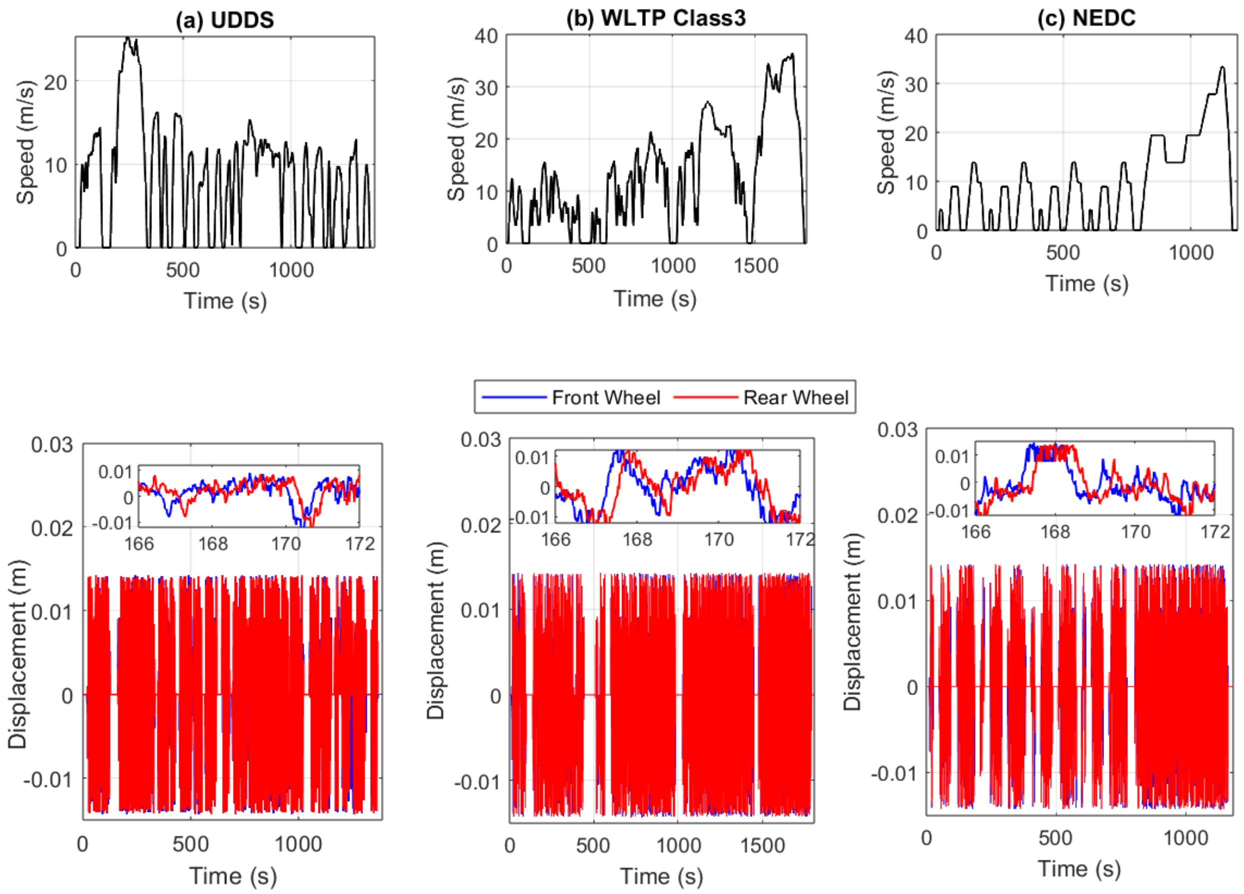

Figure 4. Speed Profiles and Wheel Road Disturbance Inputs for UDDS, WLTP Class 3, and NEDC Drive Cycles

[DOI: 10.22068/ase.2026.750]

Table 2: Comparison of UDDS, NEDC, and WLTP Class 3 Driving Cycles

Drive cycle	Duration (s)	Distance (km)	Maximum speed (km/h)	Average speed incl. stops (km/h)	Stop/idle duration (s)	Approx. stop-start events
UDDS	1369	12.07	91.25	31.5	≈ 220–260	≈ 17
NEDC	1180	10.93	120	33.35	267	≈ 14
WLTP Class3	1800	23.27	131.3	≈ 46.5	242	≈ 15

3. Modelling and Control Procedure for the Active Suspension System

The active suspension is evaluated with a full-car model rather than an isolated single-wheel model. This choice keeps the vertical translation of the vehicle body and its pitch and roll rotations in the simulation, which are the main body motions used in ride-comfort assessment (see Figure 5).

Using generalized coordinates, the full-vehicle equations are rewritten in the following compact form:

$$M_v\ddot{q} + C_v\dot{q} + K_v q = B_u u + B_r r \qquad (5)$$

$$x = [q^T\ \dot{q}^T]^T,\quad q = [z_s\ \theta\ \varphi\ z_{u,i}]^T \qquad (6)$$

Here, M_v, C_v, and K_v are the assembled inertia, damping, and stiffness matrices. $B_u$distributes the actuator inputs, while B_r introduces the road disturbances at the four tires. The vector q contains body bounce, pitch, roll, and the unsprung-mass vertical coordinates; the state vector x is obtained by appending the corresponding velocities. All motions are defined with respect to the static equilibrium position.

$$\delta_{t,fr} = z_{u,fr(t)} - z_{r,fr(t)} \qquad (7)$$

$$F_{t,fr} = k_{t,fr(t)}\delta_{t,fr}\ H(\Delta_{0,fr} - \delta_{t,fr}) \qquad (8)$$

where $k_{t,fr(t)}$ is the tire stiffness, $z_{u,fr(t)}$ is the front-right unsprung displacement, $z_{r,fr(t)}$ is the road displacement, $\Delta_{0,fr}$,fr is the static deflection limit, and H is the contact indicator function.

For control design, the full-car model is interpreted as four suspension channels located at the vehicle corners. The actuator force is generated locally at each corner so that the force transmitted from the wheel assembly to the sprung body is reduced (please see Figure 6). By lowering these corner forces, the combined excitation responsible for bounce, pitch, and roll acceleration is also reduced.

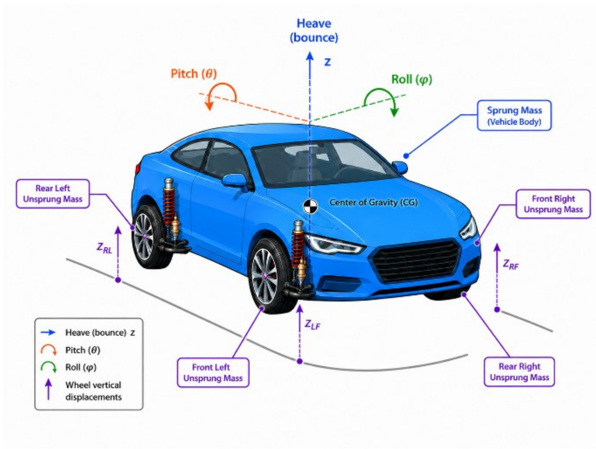

Fig. 5: Full-vehicle active suspension model

The controller therefore follows a skyhook-type concept at the four suspension locations. For each local channel, the skyhook command is written as:

$$u_{sh}(t) = -c_{sh}\dot{z}_s(t) \qquad (9)$$

where u_{sh} is the actuator command and c_{sh} is the selected skyhook damping gain. Introducing the relative suspension and tire deflections,

$$\delta_s = z_s - z_u\ ,\quad \delta_t = z_s - z_0\ , \dot{\delta}_s = \dot{z}_s - \dot{z}_u \qquad (10)$$

[DOI: 10.22068/ase.2026.750]

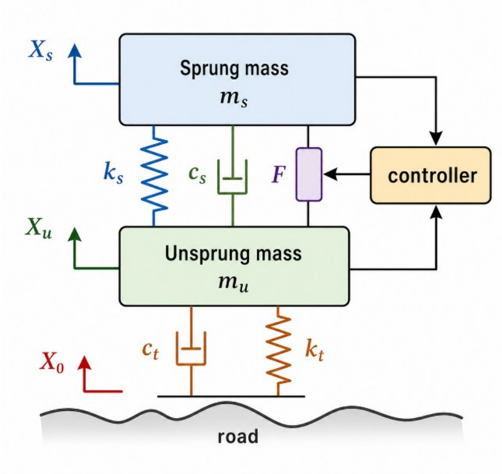

Figure 6. Equivalent quarter-car active suspension channel

Table 3: Main parameters of the active suspension model

Parameter	Symbol	Front / Rear value	Unit
Sprung mass	(m)	1376	kg
Roll / pitch moment of inertia	(I_x/I_y)	484 / 2344	kg·m²
Unsprung mass	(m_s / m_u)	40 / 40	kg
Tire stiffness	($k_{t,fr}, k_{t,r}$)	(182087 / 182087)	N/m
Suspension stiffness	($k_{s,fr}, k_{s,r}$)	10492/9560	N/m
Suspension damping	($c_{s,fr}, c_{s,r}$)	500 / 500	N·s/m

the quarter-car dynamics become:

$$m_s\ddot{z}_s(t) + c_s\,\dot{\delta}_s(t) + k_s\delta_s(t) + u_a(t) = 0 \quad (11)$$

$$m_u\ddot{z}_u(t) - c_s\,\dot{\delta}_s(t) - k_s\delta_s(t) + k_t\delta_t(t) - u_a(t) = 0 \quad (12)$$

In these equations, m_s and m_u are the sprung and unsprung masses. The parameters k_s, c_s, and k_t are the suspension stiffness, suspension damping, and tire stiffness, respectively. The displacements z_s, z_u, and z_0 denote the sprung mass, unsprung mass, and road input, while u_a acts between the two masses according to the selected sign convention.

In the active-suspension case, the passive spring stiffness is reduced to 0.75 of its nominal value. The signed instantaneous actuator power is then obtained from the product of actuator force and relative actuator velocity:

$$P_a(t) = u_a(t)v_a(t)\,, \qquad v_a(t) = \dot{z}_s(t) - \dot{z}_u(t) \qquad (13)$$

$$P_a(t) = -c_{sh}\dot{z}_s(t)[\dot{z}_s(t) - \dot{z}_u(t)] \qquad (14)$$

Positive P_a indicates that the actuator injects mechanical power into the suspension, whereas negative P_a indicates energy absorption by the actuator. The main specifications of the full-car and equivalent quarter-car active suspension models are presented in Table 3.

4. Optimization Framework and GA-Based Fuzzy Active Suspension Control

Figure 7 presents the proposed simulation and optimization framework for a pure electric vehicle equipped with an active suspension system. The driving cycle is applied as the main longitudinal input to the electric vehicle model, while the road disturbance profile is imposed on the active suspension model to represent vertical excitation from the road surface. The vehicle model calculates the battery operating conditions, such as current demand, state of charge, temperature, and charge throughput, which are used to evaluate battery aging. At the same time, the active suspension model provides the vehicle body dynamic responses, including bounce, pitch, and roll accelerations, which are used to quantify ride comfort. Therefore, the framework connects the energy storage behavior of the electric powertrain with the vertical dynamic response of the suspension system. The final optimization target is formulated as a single-objective cost function that simultaneously considers battery degradation and ride comfort performance.

The fuzzy active suspension controller is optimized using a genetic algorithm (GA). In each generation, the GA produces a new set of

[DOI: 10.22068/ase.2026.750]

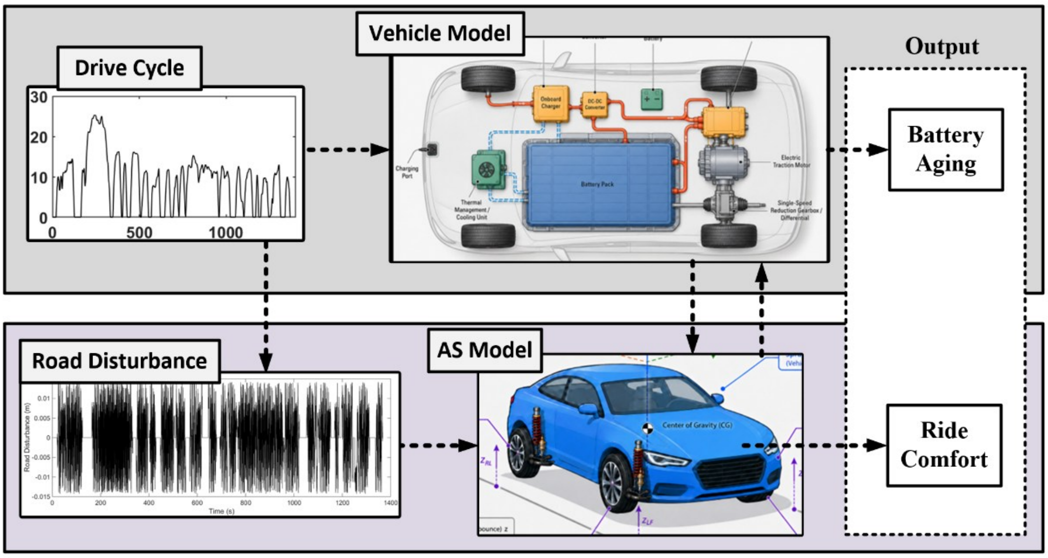

Fig. 7. Proposed EV–Active Suspension Simulation and Optimization Framework

membership function parameters for the fuzzy controller inputs and output. These parameters are applied to the controller, the complete EV–active suspension Simulink model is executed, and the resulting vehicle responses are used to evaluate the objective function. The optimization criterion combines ride comfort,

After applying the human vibration weighting filters, the RMS values of the filtered acceleration signals are calculated as:

$$a_{z,\ rms} = \sqrt{mean(a_{z,\ w}^2)} \tag{15}$$

$$a_{\theta,\ rms} = \sqrt{mean(a_{\theta,\ w}^2)}$$

$$a_{\varphi,\ rms} = \sqrt{mean(a_{\varphi,\ w}^2)}$$

where a_z, $a_{\theta,}$, and a_φ are the filtered bounce, pitch, and roll acceleration signals, respectively. The overall ride comfort index is then defined as:

$$RI = \sqrt{a_{z,\ rms}^2 + a_{\theta,\ rms}^2 + a_{\varphi,\ rms}^2} \tag{16}$$

where RI represents the ride comfort index. A lower RI indicates improved passenger comfort. The weighting factors 0.4 and 0.63 account for the relative influence of pitch and roll accelerations compared with vertical bounce acceleration. Ride comfort is evaluated using a frequency-weighted RMS acceleration

suspension travel, final battery state of charge, and battery aging into a single normalized cost function.

Ride comfort is evaluated from the weighted bounce, pitch, and roll accelerations of the vehicle body.

approach inspired by ISO 2631-1, which is widely used for assessing human exposure to whole-body vibration. In this method, the vehicle body bounce, pitch, and roll acceleration responses are filtered using human-sensitivity weighting functions before calculating their RMS values. The resulting weighted acceleration components are then combined into a single ride comfort index. This approach allows the optimization process to consider not only the magnitude of vibration but also its frequency content, which is important because the human body is more sensitive to vibration in specific frequency ranges.

The final optimization objective is formulated as a weighted sum of five normalized terms:

$$J = w_1\left(\frac{RI}{\overline{RI}}\right) + w_2\left(\frac{max|ST_{fr}|}{\overline{ST}_{fr}}\right) + w_3\left(\frac{max|ST_{rr}|}{\overline{ST}_{rr}}\right) + w_4\left(\frac{1-SOC_{end}}{SOC_{int}}\right) + w_5\left(\frac{Q_{loss}}{\overline{Q}_{loss}}\right) \tag{16}$$

[DOI: 10.22068/ase.2026.750]

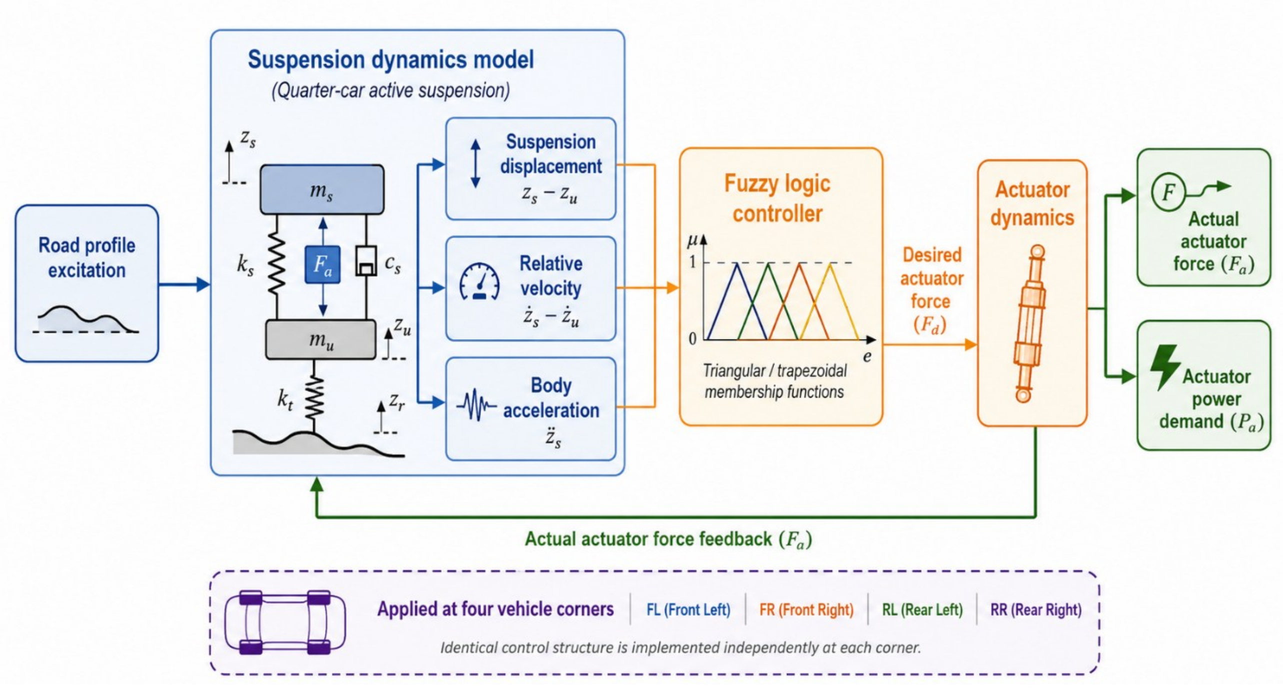

Fig. 8. Fuzzy Active Suspension Control Architecture with Actuator Dynamics and Power Evaluation

In this formulation, ST_{fr} and ST_{rr} denote the front and rear suspension travel responses, respectively, SOC_{end} is the final battery state of charge, and Q_loss is the calculated battery capacity loss. Moreover, $(\overline{ST_{fr}})$ and $(\overline{ST_{rr}})$ indicate the reference values used for normalizing the front and rear suspension travel responses, respectively, whereas $(\overline{Q_{loss}})$ represents the reference value adopted for normalizing the battery aging term. As shown in Figure 8, the active suspension system is controlled by four identical fuzzy logic controllers, each assigned to one vehicle corner: front-left, front-right, rear-left, and rear-right.

Each fuzzy controller consists of two normalized inputs and one normalized output. All variables are scaled within the interval ([-1,1]) and are described using five linguistic sets: negative big (NB), negative small (NS), zero (ZE), positive small (PS), and positive big (PB). As illustrated in Figure 9, the boundary membership functions, NB and PB, are trapezoidal, while the intermediate sets, NS, ZE, and PS, are triangular. This structure provides smooth transitions between control regions and prevents sudden changes in the commanded actuator force.

The fuzzy membership functions are tuned using a genetic algorithm. The optimization vector is divided into three parts: (p1) for the first input, (p2) for the second input, and (o) for the output membership functions. During each optimization step, the membership breakpoints are updated, the EV–active suspension Simulink model is executed, and the objective function is evaluated based on ride comfort, suspension travel, final battery state of charge, and battery capacity loss. Therefore, the controller is optimized not only to improve vibration isolation, but also to reduce the adverse effect of active suspension operation on battery performance.

[DOI: 10.22068/ase.2026.750]

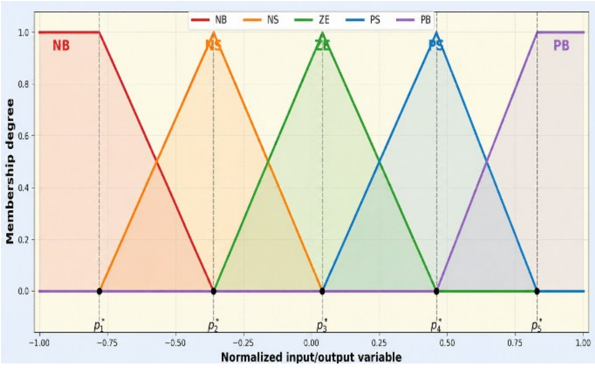

Figure 9. Initial Fuzzy Membership Functions for the Active Suspension Controller

The fuzzy rule base was defined based on the physical behavior of the active suspension and the adopted skyhook-type concept. The normalized inputs d and Dd, and output u, are represented by five linguistic sets (NB, NS, ZE, PS, and PB), forming the 25 rules summarized in Table 4. The rule base is kept fixed, while the GA optimizes the input and output membership functions to reduce computational cost. Although the rules themselves remain unchanged, the optimized membership functions modify their firing strengths and relative contributions, thereby changing the effective fuzzy control surface.

Table 4. Fuzzy rule base used for the active suspension controller

	NB	**NS**	**ZE**	**PS**	**PB**
NB	PB	PS	ZE	ZE	NS
NS	NB	NS	NS	NS	NS
ZE	NS	ZE	ZE	ZE	PS
PS	ZE	ZE	PS	PS	PB
PB	PS	ZE	ZE	NS	NB

5. Results and discussion

Figure 10 illustrates the convergence behavior of the genetic algorithm used to optimize the fuzzy active suspension controller under three driving cycles. In Figure 10(a), the UDDS cycle shows a rapid reduction in the objective function during the first generations, where the best fitness decreases from about 2.72 to 2.65, and then gradually stabilizes.

The final best and mean fitness values are very close, equal to 2.64913 and 2.64914, respectively, indicating good convergence of the population. A similar trend is observed for the NEDC cycle in Figure 10(b), where the fitness value decreases quickly in the early generations and reaches the lowest final objective value among the three cycles, with a best fitness of 2.33852 and a mean fitness of 2.33854. This lower value can be related to the smoother and less aggressive nature of the NEDC profile compared with UDDS and WLTP. In contrast, Figure 10(c) shows that the WLTP cycle has the highest final fitness value, 2.71036, which reflects the more demanding driving condition, wider speed range, and stronger excitation effects on the EV–active suspension system. The lower subplots provide a detailed view of the population distribution and best-score evolution at the final stage of the GA process. As shown in Figure 10(d), Fig. 10(e), and Fig. 10(f), the population scores are distributed around the final optimum, while the red best-score curves remain nearly stable after convergence. This behavior confirms that the GA successfully identifies optimized fuzzy-controller parameters for each driving cycle. The small difference between the best and mean fitness values in all cases also shows that the population has converged consistently, and the optimized controller provides a stable compromise between ride comfort, suspension travel, final battery state of charge, and battery degradation, which are the main terms of the proposed objective function.

Furthermore, Figure 11 shows the optimized and non-optimized membership functions of the fuzzy active suspension controller for the three driving cycles.

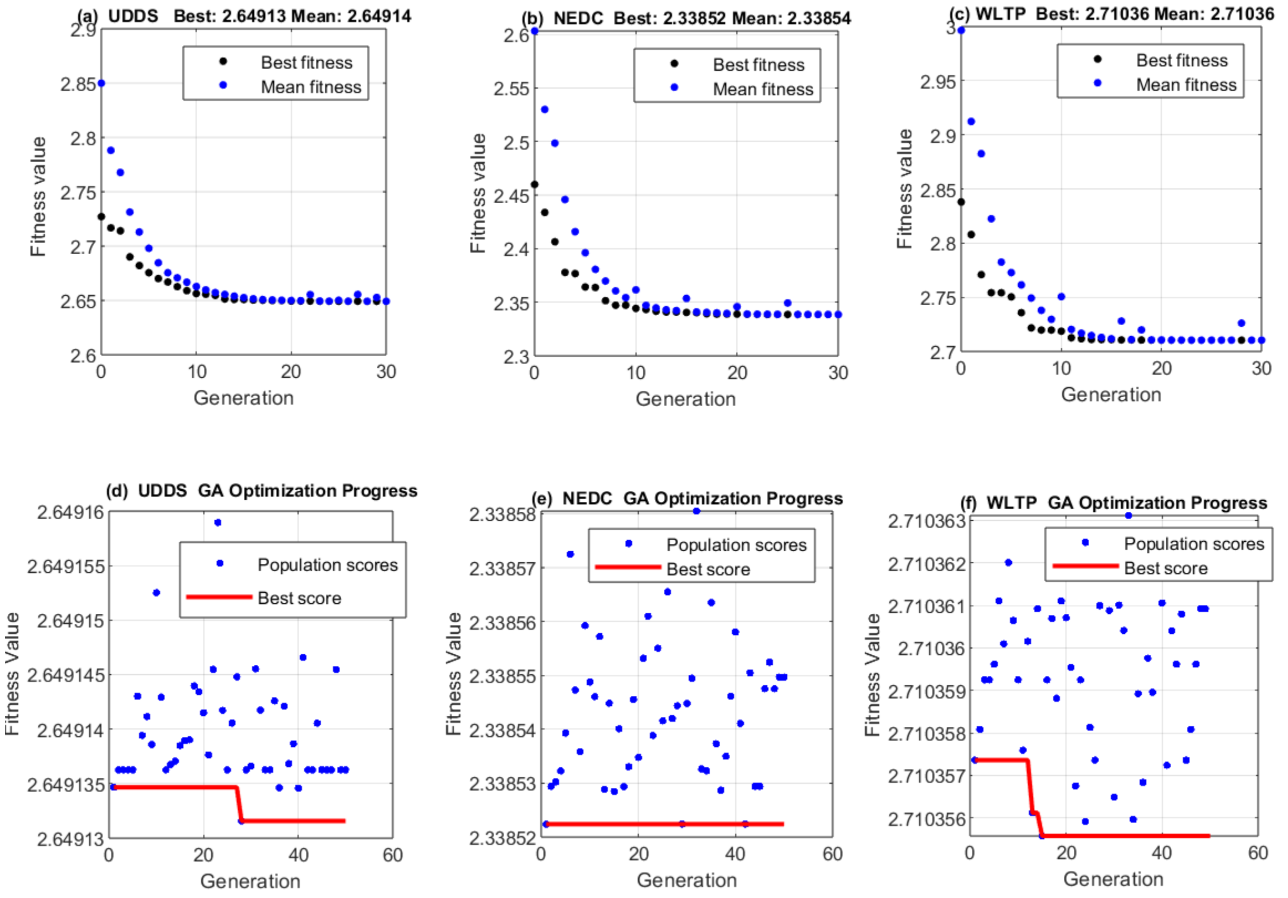

Fig. 10. Convergence History of the Genetic Algorithm Optimization under UDDS, NEDC, and WLTP Driving Cycles

Subplots (a)–(c) correspond to UDDS, (d)–(f) to NEDC, and (g)–(i) to WLTP, where the first input, second input, and output membership functions are presented separately. The dashed curves represent the initial non-optimized membership functions, while the solid curves show the GA-optimized membership functions. It can be observed that the genetic algorithm modifies the position and width of the linguistic regions NB, NS, ZE, PS, and PB according to the dynamic requirements of each driving cycle. In particular, the optimized membership functions are no longer uniformly distributed, which indicates that the controller requires different sensitivity levels in different operating regions. The changes are more noticeable in the zero and positive regions of the input and output variables, showing that the GA adjusts the fuzzy controller to improve the compromise between vibration reduction, actuator effort, suspension travel, and battery-related performance. Moreover, Figure 12 compares the active suspension power consumption and generated power for the non-optimized and optimized controllers under UDDS, NEDC, and WLTP Class 3 cycles. In Figure 12(a), the UDDS results show frequent positive and negative power fluctuations due to the stop-and-go nature of the cycle and the repeated road excitations. The optimized controller produces almost the same general power pattern as the non-optimized case, but the zoomed view shows that the consumed power is slightly reduced at several peaks. For the NEDC cycle, shown in Figure 12(b), the power demand is smoother during the early urban part and becomes more intensive near the extra-urban section, where both consumption and generation increase. The optimized case again follows the same trend while slightly decreasing the required active suspension power in the highlighted interval.

[DOI: 10.22068/ase.2026.750]

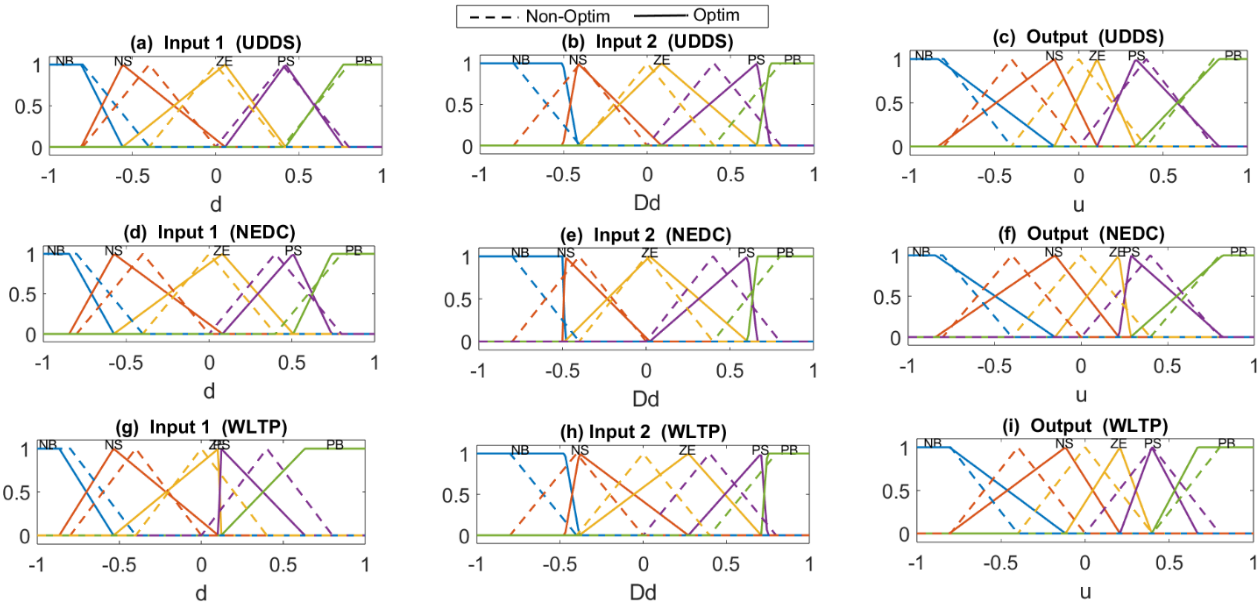

Fig. 11. Optimized and Non-Optimized Fuzzy Membership Functions for the Active Suspension Controller

In Figure 12(c), the WLTP Class 3 cycle presents stronger and more irregular power variations because of its wider speed range and more aggressive driving behavior. The zoomed subplot confirms that the optimized controller reduces some of the peak power consumption compared with the non-optimized case, while maintaining a similar generated-power response. Overall, the results indicate that the GA-optimized fuzzy controller improves the energy behavior of the active suspension mainly by reducing unnecessary power consumption without significantly decreasing the available generated power.

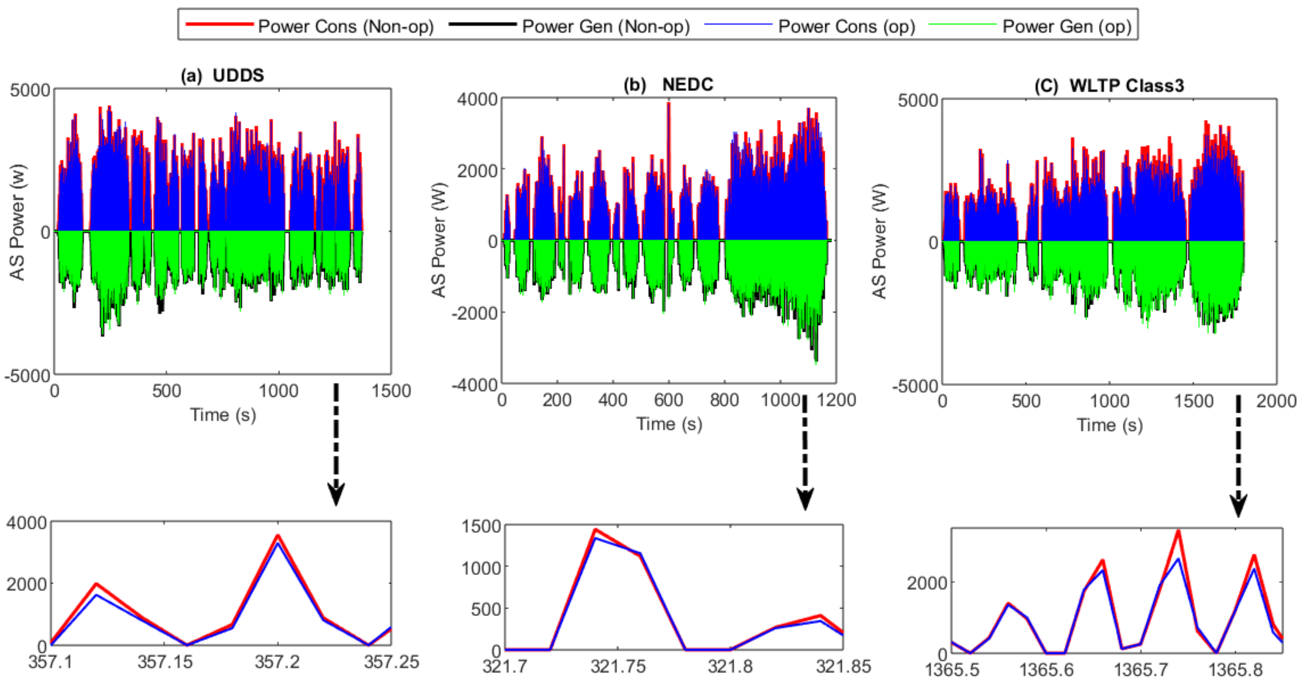

Fig. 12. Comparison of Optimized and Non-Optimized Active Suspension Power Consumption and Generated Power under Different Driving Cycles

Table 5 and Figure 13 summarize the effect of the GA-optimized fuzzy active suspension controller compared with the non-optimized case under NEDC, UDDS, and WLTP Class 3

[DOI: 10.22068/ase.2026.750]

driving cycles. In general, the optimized controller improves the main dynamic and battery-related performance indices in all three cycles. For the NEDC cycle, the improvement is the most significant: the ride comfort index decreases from 0.06117 to 0.0518, while the front and rear suspension changes are reduced from 84.0 mm to 33.5 mm and from 77.4 mm to 32.3 mm, respectively. This shows that the optimized controller strongly suppresses suspension motion under the smoother NEDC driving condition. The battery capacity loss index, Q_{BA}, is also reduced from 0.0114 to 0.0110. In the UDDS cycle, the improvements are smaller but still consistent, where the ride comfort index decreases from 0.03709 to 0.03628, the front and rear suspension changes are slightly reduced, and Q_{BA} decreases from 0.0116 to 0.0110. For the WLTP Class 3 cycle, which represents the most demanding driving condition, the optimized controller also reduces the ride comfort index from 0.03733 to 0.03645, decreases the front suspension change from 85.8 mm to 82.6 mm, and provides a more noticeable reduction in rear suspension change from 79.3 mm to 67.4 mm. Moreover, Q_{BA} decreases from 0.0131 to 0.0125, indicating that the optimized controller reduces battery degradation even under the more aggressive WLTP profile. The power results show that the optimization does not simply minimize actuator power in all cases; instead, it balances ride comfort, suspension travel, battery aging, and energy exchange.

For example, in NEDC, the average power consumption decreases from 251 W to 175.8 W, while in UDDS and WLTP it slightly increases, which suggests that a small additional actuator effort is used when needed to improve suspension and battery-aging performance. The SOC plot (see Figure 14) further supports this interpretation, showing that the optimized controller does not cause an undesirable SOC drop and maintains acceptable battery energy behavior throughout the drive cycles.

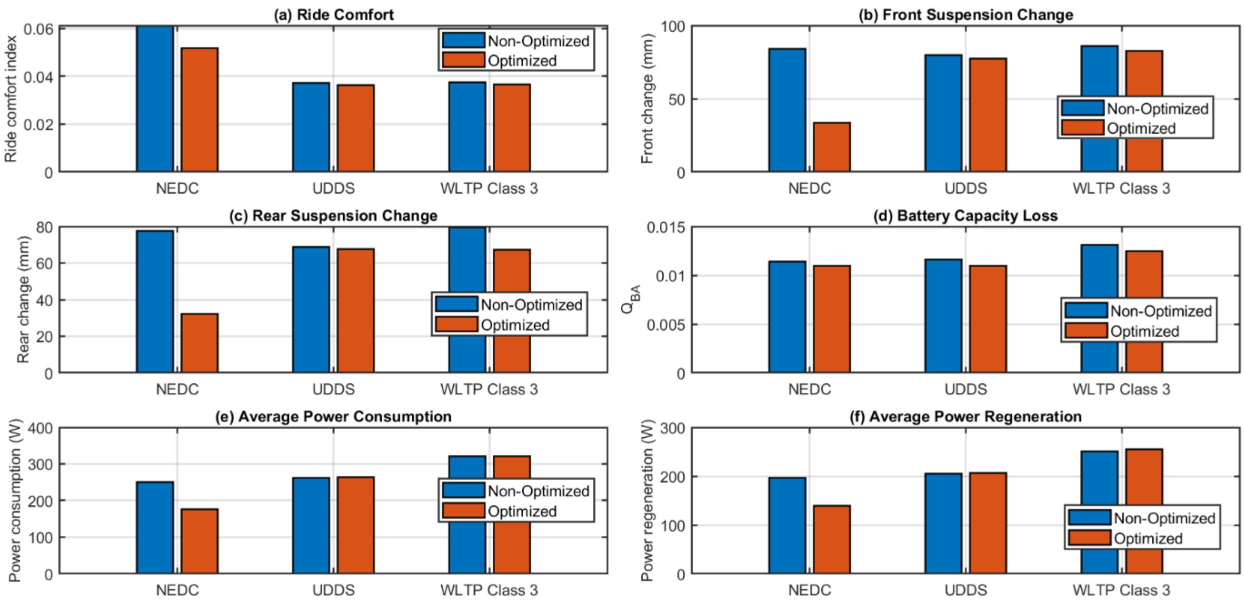

Fig.13. Comparison of Non-Optimized and GA-Optimized Active Suspension Performance Indices under NEDC, UDDS, and WLTP Class 3 Driving Cycles

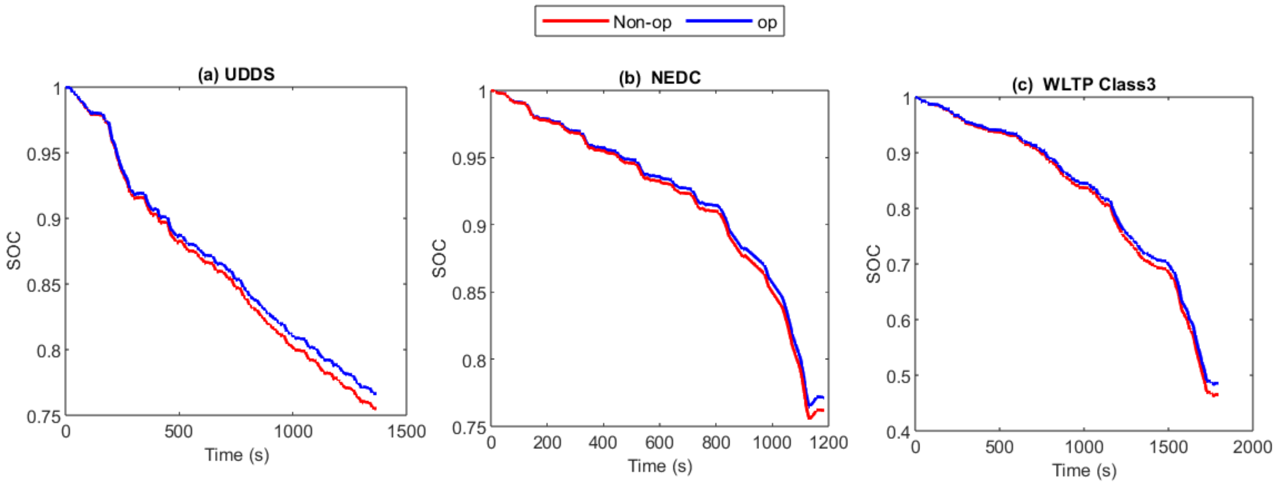

Fig. 14. Battery SOC Response of the Non-Optimized and GA-Optimized Active Suspension System under Different Driving Cycles

Therefore, the combined results from Table 5, the bar chart, and the SOC response confirm that the GA-optimized fuzzy controller achieves a better overall compromise between ride comfort, suspension motion limitation, actuator energy demand, regenerative power behavior, and battery health preservation.

Figure 15 shows the EV required power for UDDS, NEDC, and WLTP Class 3. In Fig. 15(a), UDDS has frequent power fluctuations because of repeated acceleration and braking in urban stop-and-go driving. In Fig. 15(b), NEDC shows a smoother and more regular pattern, but the required power increases sharply in the final extra-urban section. In Figure 15(c), WLTP Class 3 presents the most aggressive and variable power demand, with frequent high positive peaks and regenerative braking regions. Therefore, WLTP imposes the most demanding load on the EV powertrain, while UDDS mainly represents transient urban operation and NEDC shows smoother behavior with high power demand near the end of the cycle.

In percentage terms, the optimized controller reduces the ride-comfort index by 15.32%, 2.18%, and 2.36% and the battery-aging index by 3.51%, 5.17%, and 4.58% under NEDC, UDDS, and WLTP Class 3, respectively. The largest suspension improvements occur under NEDC, where the front and rear suspension travel decrease by 60.12% and 58.27%. The nonuniform optimized membership functions indicate that the GA redistributes controller sensitivity across different operating regions; modifications around the ZE, NS, and PS regions change the response to frequently occurring small and moderate suspension motions, while the outer regions regulate the response to larger disturbances. The optimization also reveals a trade-off between actuator effort and battery health. Under NEDC, net average suspension power decreases by approximately 31.30%, together with a 3.51% reduction in battery aging. Under UDDS, a small 2.46% increase in net suspension power is accepted while battery aging decreases by 5.17%, whereas under WLTP the net suspension power decreases by approximately 5.04% together with a 4.58% reduction in battery aging. Thus, the optimized controller does not simply minimize actuator power, but seeks a compromise among suspension performance, battery energy use, and degradation.

[DOI: 10.22068/ase.2026.750]

Table 5: Quantitative Comparison of Non-Optimized and GA-Optimized Active Suspension Performance under Different Driving Cycles

Driving Cycle	NEDC		UDDS		WLTP_Class3	
	Non_OP	OP	Non_OP	OP	Non_op	op
Comfort ride	0.06117	0.0518	0.03709	0.03628	0.03733	0.03645
Front change (mm)	84.0	33.5	79.6	77.2	85.8	82.6
Rear Change (mm)	77.4	32.3	68.9	67.5	79.3	67.4
Q_BA	0.0114	0.0110	0.0116	0.0110	0.0131	0.0125
Best op	-	2.33852	-	2.64913	-	2.71036
Mean op	-	2.33854	-	2.64914	-	2.71036
Avg of power consumption (W)	251	175.8	261.9	264.7	320.1	321.7
Avg of power regeneration (W)	197	138.7	205.1	206.5	250.1	255.23

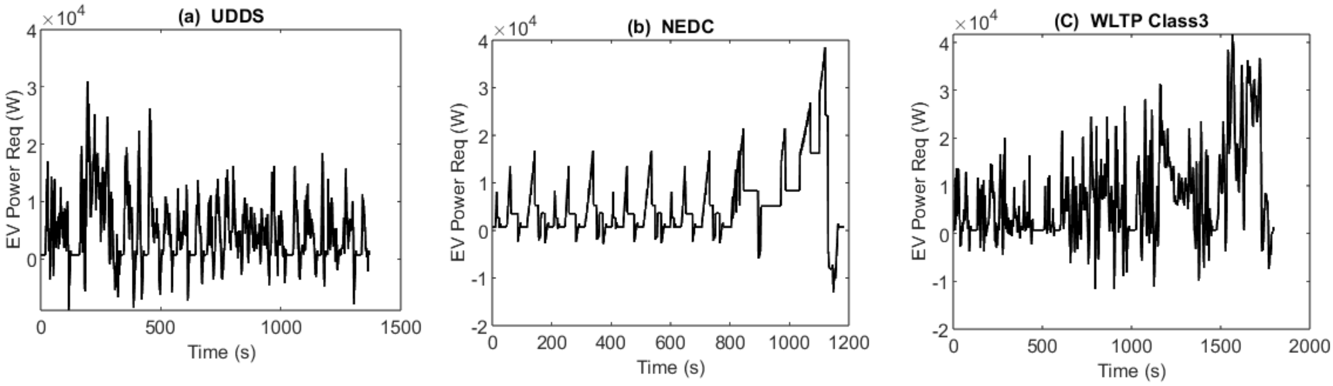

Fig. 15. Electric vehicle required power profiles for different driving cycles: (a) UDDS, (b) NEDC, and (c) WLTP Class 3.

Conclusion

In this study, a GA-optimized fuzzy active suspension controller was developed for a pure electric vehicle by considering ride comfort, suspension travel, battery SOC, and battery capacity loss. The proposed EV–active suspension framework was evaluated under UDDS, NEDC, and WLTP Class 3 driving cycles.

The results showed that the genetic algorithm successfully tuned the fuzzy membership functions for each driving condition. Compared with the non-optimized controller, the optimized controller reduced the ride comfort index, suspension displacement, and battery aging index in all cycles. The most significant improvement was observed in the NEDC cycle, where the ride comfort index decreased from 0.06117 to 0.0518, and the front and rear suspension changes were greatly reduced. In addition, (Q_{ba}) decreased in NEDC, UDDS, and WLTP Class 3, confirming the positive effect of the proposed controller on battery health.

Overall, the GA-optimized fuzzy controller provides a better compromise between passenger comfort, suspension performance, actuator energy demand, and battery degradation. Future work can focus on real road data, actuator constraints, battery thermal effects, and experimental validation.

[DOI: 10.22068/ase.2026.750]

References:

[1] Montazeri-Gh, M. and Mostashiri, A., 2025. AI-Based Multi-Objective Optimization of Fuzzy Type-2 EMS and Safe-Distance Control for an FCHEV Under Realistic Traffic Conditions. *IEEE Access*, *13*, pp.211010-211030.

[2] Mostashiri, A. and Montazeri-Gh, M., 2026. Hybrid reinforcement learning optimization of aging aware energy management and powertrain sizing in fuel cell hybrid electric vehicles. *Scientific Reports*, *16*(1), p.4166.

[3] Kelly, J.C., Elgowainy, A., Isaac, R., Ward, J., Islam, E., Rousseau, A., Sutherland, I., Wallington, T.J., Alexander, M., Muratori, M. and Franklin, M., 2023. *Cradle-to-grave lifecycle analysis of US light-duty vehicle-fuel pathways: a greenhouse gas emissions and economic assessment of current (2020) and future (2030-2035) technologies* (No. ANL--22/27-Rev. 1). Argonne National Laboratory (ANL), Argonne, IL (United States).

[4] Montazeri, G.M., Zakizadeh, M.A. and Mostashiri, A., 2025. Durability-Driven Energy Management for Fuel Cell Hybrid EVs: Multi-Scenario Optimization Across Different Traffic and Driving Cycles.

[5] Han, S.Y. and Liang, T., 2022. Reinforcement-learning-based vibration control for a vehicle semi-active suspension system via the PPO approach. *Applied Sciences*, *12*(6), p.3078.

[6] Li, Q., Chen, Z., Song, H. and Dong, Y., 2024. Model predictive control for speed-dependent active suspension system with road preview information. *Sensors*, *24*(7), p.2255.

[7] Chen, G., Du, G., Xia, J., Xie, X. and Wang, Z., 2024. Aperiodic Sampled-Data $ H_ {\infty} $ Control of Vehicle Active Suspension System: An Uncertain Discrete-Time Model Approach. *IEEE Transactions on Industrial Informatics*, *20*(4), pp.6739-6750.

[8] Wang, Y., Dong, L., Chen, Z., Sun, M. and Long, X., 2024. Integrated skyhook vibration reduction control with active disturbance rejection decoupling for automotive semi-active suspension systems. *Nonlinear Dynamics*, *112*(8), pp.6215-6230.

[9] Viadero-Monasterio, F., Boada, B.L., Zhang, H. and Boada, M.J.L., 2023. Integral-based event triggering actuator fault-tolerant control for an active suspension system under a networked communication scheme. *IEEE Transactions on Vehicular Technology*, *72*(11), pp.13848-13860.

[10] Emami, A., Masih-Tehrani, M., Amirkhani, A. and Najafi, A., 2025. Robust Fuzzy Sliding Mode Controller for the Full Vehicle Semi-Active Suspension System Considering the Impact of Uncertainties. *IET Intelligent Transport Systems*, *19*(1), p.e70125.

[11] Gheibollahi, H., Masih-Tehrani, M. and Najafi, A., 2024. Improving ride comfort approach by fuzzy and genetic-based PID controller in active seat suspension. International Journal of Automation and Control, 18(2), pp.184-213.

[12] Salehpour, M., Jamali, A., Bagheri, A. and Nariman-Zadeh, N., 2018. Optimum Pareto design of vehicle vibration model excited by non-stationary random road using multi-objective differential evolution algorithm with dynamically adaptable mutation factor. ASE 2018; 8 (4) :2854-2867

[13] Salehpour, M. and Bagheri, A., 2021. Pareto optimization of a nonlinear vehicle model using multi-objective differential evolution algorithm with fuzzy inference-based adaptive mutation factor (MODE-FM). *Automotive Science and Engineering*, *11*(3), pp.3594-3613.

[14] Salehpour, M., Jamali, A., Bagheri, A. and Nariman-Zadeh, N., 2017. Optimum sliding mode controller design based on skyhook model for nonlinear vehicle vibration model. *International Journal of Automotive Engineering*, *7*(4), pp.2537-2550.

[15] Mosammam, Z.M., Ahmadi, P. and Houshfar, E., 2024. Multi-objective optimization-driven machine learning for charging and V2G pattern for plug-in hybrid vehicles: Balancing battery aging and power management. *Journal of Power Sources*, *608*, p.234639.

[16] Bamdezh, M.A. and Molaeimanesh, G.R., 2024. Aging behavior of an electric vehicle battery system considering real drive conditions. *Energy Conversion and Management*, *304*, p.118213.

[17] Pozzato, G., Allam, A. and Onori, S., 2022. Lithium-ion battery aging dataset based on electric vehicle real-driving profiles. *Data in brief*, *41*, p.107995.

[18] Li, X. and Chu, J., 2025. Lithium battery life prediction for electric vehicles using enhanced TCN and SVN quantile regression. *IEEE Access*, *13*, pp.12581-12595.

[19] Montazeri-Gh, M. and Soleymani, M., 2009. Investigation of the energy regeneration of

[DOI: 10.22068/ase.2026.750]

active suspension system in hybrid electric vehicles. *IEEE transactions on industrial electronics*, *57*(3), pp.918-925.

[20] Shi, D., Pisu, P., Chen, L., Wang, S. and Wang, R., 2016. Control design and fuel economy investigation of power split HEV with energy regeneration of suspension. *Applied Energy*, *182*, pp.576-589.

[21] Pham, T.H., Jacob, J., Wilkins, S., Lauwerys, C. and Dhaens, M., 2017, April. Integrated model for battery Electric Vehicles with energy harvesting active suspension system. In *2017 Twelfth International Conference on Ecological Vehicles and Renewable Energies (EVER)* (pp. 1-10). IEEE.

[22] Long, G., Ding, F., Zhang, N., Zhang, J. and Qin, A., 2020. Regenerative active suspension system with residual energy for in-wheel motor driven electric vehicle. *Applied Energy*, *260*, p.114180.

[23] Bakar, S.A.A., Masuda, R., Hashimoto, H., Inaba, T., Jamaluddin, H., Rahman, R.A. and Samin, P.M., 2012. Active suspension system in improving ride and handling performance of electric vehicle conversion. *International Journal of Electric and Hybrid Vehicles*, *4*(1), pp.24-53.

[24] Markel, T., Brooker, A., Hendricks, T., Johnson, V., Kelly, K., Kramer, B., O'Keefe, M., Sprik, S. and Wipke, K., 2002. ADVISOR: a systems analysis tool for advanced vehicle modeling. *Journal of power sources*, *110*(2), pp.255-266.

[25] Montazeri-Gh, M. and Mostashiri, A., 2025. AI-driven multi-objective optimization of FCHEV sizing and energy management considering degradation and vehicle dynamics under realistic machine learning-based traffic conditions. *Scientific Reports*, *15*(1), p.39873.

[26] Cordoba-Arenas, A., Onori, S. and Rizzoni, G., 2015. A control-oriented lithium-ion battery pack model for plug-in hybrid electric vehicle cycle-life studies and system design with consideration of health management. *Journal of Power Sources*, *279*, pp.791-808.

[27] Esfahanian, M., Mahmoodian, A., Amiri, M., MASIH, T.M., Nehzati, H., Hejabi, M. and Manteghi, A., 2013. Large lithium polymer battery modeling for the simulation of hybrid electric vehicles using the equivalent circuit method. *International Journal of Automotive Engineering.* Vol. 3 (4).

[28] Montazeri-Gh, M., Zakizadeh, M.A., Mostashiri, A. and Chini, A., 2026. Investigation of efficient optimization algorithms for durability-aware energy management for fuel cell hybrid electric vehicles across real-world traffic conditions. *International Journal of Modelling and Simulation*, pp.1-23.

[DOI: 10.22068/ase.2026.750]